Mean Velocity Field Relative to a Rushton Turbine Blade

Carl M. Stoots and Richard V. Calabrese
Dept. of Chemical Engineering, University of Maryland, College Park, MD 20742

The 3-D flow field relative to a rotating Rushton turbine blade is acquired for fully turbulent tank conditions by synchronizing LDA measurements with the output of a shaft-mounted encoder. This makes it possible to capture the impeller stream velocity field, including the details of the vortices behind the blades. Mean velocity data at three impeller speeds show the extent of periodicity and the axes and structure of the vortices. Pumping capacities are determined and it is shown that the radial jet is a consequence of fluid entrainment into the vortices. Deformation rates based on gradients of mean velocity are calculated. Close to the blade they can exceed impeller rotational frequency by as much as two orders of magnitude. To a first approximation, the normalized mean flow field is independent of impeller speed.

Introduction

The development of accurate turbulent mixing and scaleup models for stirred-tank reactors has been limited by a lack of understanding of the three-dimensional turbulent velocity characteristics in such vessels. This is particularly true for the discharge flow of the impeller, characterized by periodic velocity fluctuations, high three dimensionality, and the existence of well defined vortical structures. Because the complexity of this flow field makes theoretical work extremely difficult, most related studies have been experimental. The studies of flows generated by disc turbines were reviewed excellently by Ranade and Joshi (1990).

The dominant features of the flow field near a Rushton turbine depend on the perspective or frame of reference from which it is viewed. Figure 1a represents the customary way in which the flow field is measured: a stationary measurement probe and rotating impeller with measurements taken relative to a fixed set of coordinates. This will be termed a fixed frame of reference. Measurements taken from this perspective show a periodic component (see Figure 1b), termed pseudo-turbulence by van't Riet et al. (1976), superimposed upon the background turbulence with a frequency of periodicity corresponding to the passage of successive impeller blades. The resultant energy spectra likewise show a peak at this same frequency (Mujumdar et al., 1970; Rao and Brodkey, 1972; Gunkel and Weber, 1975). Researchers have employed various mathematical as well as experimental means to remove or correct for this pseudo-turbulence in their measurements. Rao and Brodkey (1972) graphically separated the periodic contributions from their autocorrelations. Wu and Patterson (1989) performed a similar subtraction of the periodic contributions from the autocorrelation function by representing the periodicity as a two-term Fourier series where the two terms represent the blade passage frequency and the first higher-order harmonic.

A second frame of reference may be defined, one which rotates with the impeller and is relative to the impeller blade (Figure 2a). Measurements taken in a rotating frame of reference reveal a very different flow field near the impeller than those taken in a fixed frame. The periodicity of measurements taken in the fixed frame now corresponds to the acceleration and deceleration of the fluid as it passes over successive blades. Furthermore, well-defined fluid structures emerge in the form of trailing vortices, as shown in Figure 2b. Some experimental measurements have been made in this rotating frame of reference. Van't Riet and Smith (1973, 1975) mounted a camera on a turntable below the stirrer. By rotating this turntable at the impeller rate, pictures of tracer particles were taken relative to the spinning impeller. Concentrating on the trailing vortices, they measured the position of the vortex axis, angular and circumferential mean velocities within the vortices, and the pressure distribution.

Correspondence concerning this article should be addressed to R. V. Calabrese.
The current address of C. M. Stoots is: Idaho National Engineering Laboratory, P.O. Box 1625, Idaho Falls, ID 83415.

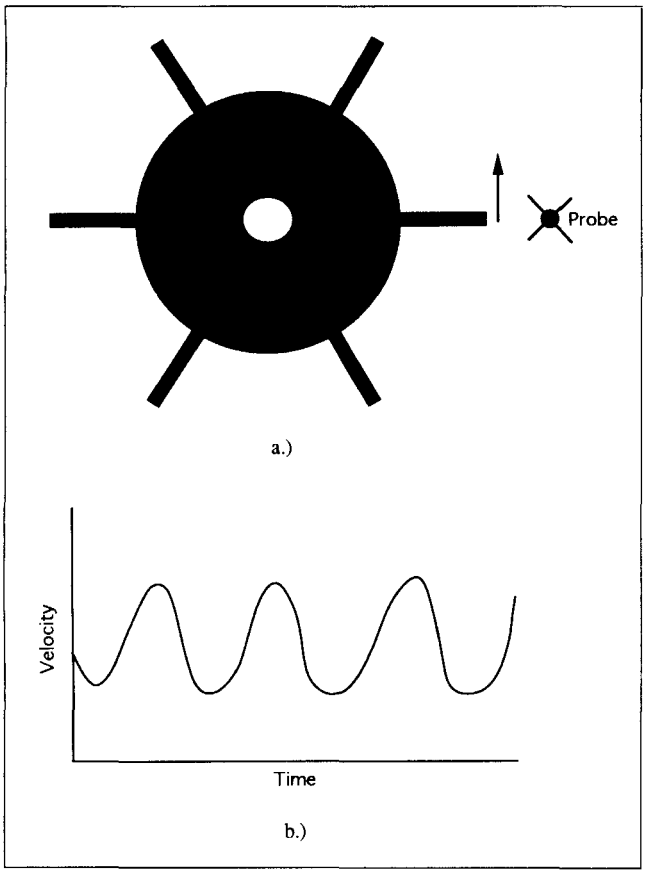

Figure 1. Fixed frame of reference.
(a) Fixed probe; (b) velocity trace.

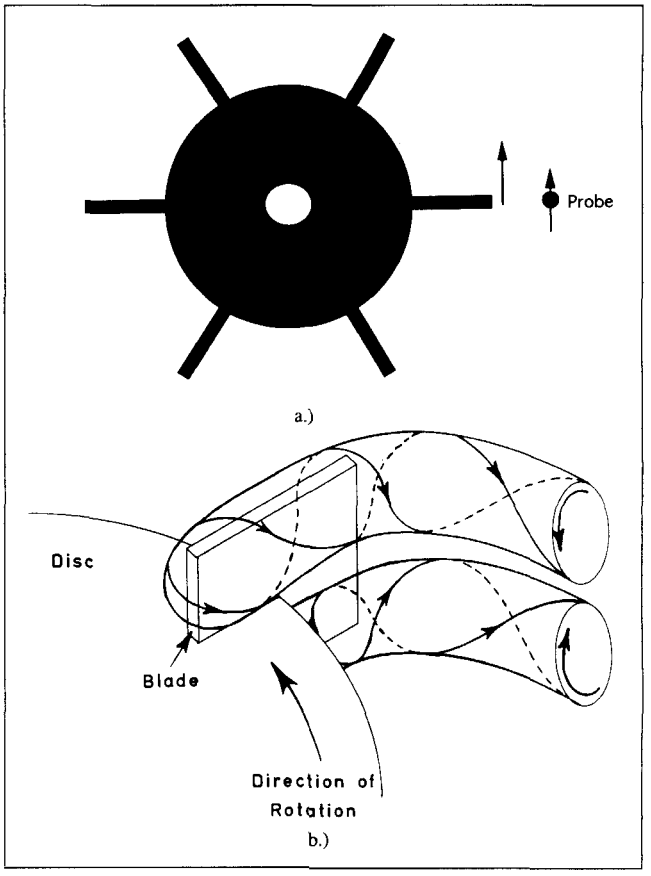

Figure 2. Rotating frame of reference.
(a) Probe rotating with impeller; (b) trailing vortices behind turbine blade (after van't Riet and Smith (1975)).

Gunkel and Weber (1975) mounted a hot wire directly on the rotating impeller and measured mean and fluctuating velocities and pumping capacities. However, their reported pumping capacities are 20% higher than those reported by other authors. This may be due to their larger impeller to tank diameter ratio, the presence of the probe, or the use of air, rather than a liquid as the working fluid. Yianneskis et al. (1987) synchronized their laser-Doppler anemometer (LDA) measurements with a predesignated stirrer shaft angle through the use of a shaft encoder. In this way they could contrast the measured flow fields obtained from the fixed and rotating frames of reference. By ensemble-averaging their velocity measurements with shaft angle they found that the trailing vortices maintained their identity for up to 20° displacement from the blade. In a previous article outlining their velocity measurement technique, however, Melling and Whitelaw (1976) acknowledged that considerable errors can arise in at least one component of mean velocity using their approach in which sampling was performed at three different orientations of the optical axis to acquire all three components of velocity.

The objectives of this study were to elucidate the impeller stream flow field and trailing vortex system for a Rushton turbine in water in a frame of reference rotating with the impeller. A two-component LDA, in conjunction with an optical shaft encoder, was used to measure three components of angularly-correlated mean and rms velocities. These measurements were performed at three impeller rotation rates. Mean velocities relative to the blade are presented in the form of vector plots and the shape and axis of the trailing vortices are calculated. The spatial extent of periodicity within the vessel and the pumping capacity of the impeller are discussed, as well as deformation rates due to mean velocity gradients within the impeller stream. The data set provides a detailed physical picture of impeller stream hydrodynamics, impeller boundary conditions, and a basis for validation of computational fluid dynamics codes.

Experimental Technique

Measurements were obtained in a cylindrical tank of plexiglas construction with an inside diameter T = 29.9 cm and wall thickness of 0.64 cm. The tank included four equally spaced baffles of width $T/10$. The tank was filled with deionized water to a height T. To minimize noise in the LDA signals, the water was passed through a 0.2-μm filter and then seeded with 5-μm polystyrene particles supplied by Duke Scientific, Inc. To minimize optical distortion of the laser beams due to index of refraction mismatch, the cylindrical vessel was placed within a larger, water-filled plexiglas box. The tank and turbine systems used are shown in Figure 3. The impeller was a standard Rushton turbine with $D = T/3$. Table 1 gives the various dimensions of the impeller used in this study. Importantly, the

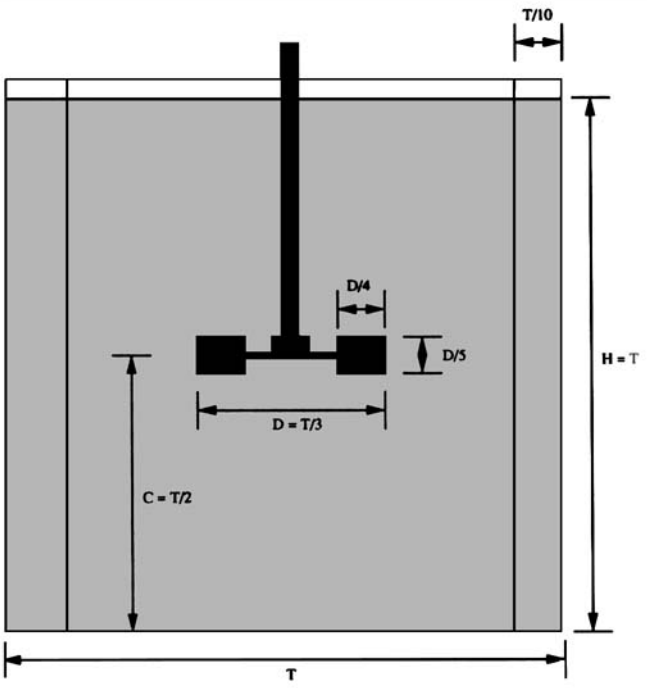

Figure 3. Stirred tank and Rushton turbine.

impeller has a relatively large hub and neither the hub nor the stirrer shaft protrudes from the bottom of the turbine disc. The turbine was located with a clearance of $T/2$ from the bottom of the vessel. The impeller was driven by a variable speed electric motor. The entire tank and motor assembly was mounted on a single-axis traversing platform.

The LDA employed in this study was developed by Dantec Electronics and operated in the backscatter mode. The system consists of a 5-W Spectra-Physics argon-ion laser, two-color 55X modular optics, two counter processors, and two frequency shifters. The front focusing lens had a focal length of 31 cm and produced a beam intersection angle of 9.92°. Additional equipment included a fully automated two-axis traversing system, buffer interface, and a signal coincidence filter. The use of the LDA traversing system in conjunction with the vessel traversing platform allowed positioning of the measurement location anywhere within the vessel. Data collected by the LDA were transferred in real time via Dantec supplied software to a Digital Equipment Corporation PDP 11/73 computer equipped with a 33 megabyte hard disc. The computer also controlled certain LDA settings and the two-directional traversing system. Both frequency shifters were set at 0.4 MHz. The low pass filter settings were 1 MHz and the high pass filter settings were 0.016 MHz. These settings allowed the measurement of velocities in the range of +5 to −4 m/s. The experimental vessel, LDA optics, and electronics were contained in an air conditioned and dehumidified room at 20°C.

Table 1. Rushton Turbine Impeller Dimensions

Impeller diameter = 10.1 cm	Disc diameter = 6.2 cm
Blade length = 2.5 cm	Disc thickness = 0.32 cm
Blade width = 2.0 cm	Hub diameter = 2.5 cm
Blade thickness = 0.32 cm	Hub height = 1.7 cm

Using a shaft mounted encoder to monitor the Rushton turbine angular position, rotating frame measurements were acquired. Once per revolution the signal from the optical encoder triggers a dual timing board (DTB) in the LDA electronics to reset. The DTB measures the time between resets as well as the time at which each velocity realization is obtained. These are used to calculate the location of each stirrer blade relative to the fixed sampling location for each data point so that in the data file each instantaneous velocity is assigned an angular position relative to a reference blade. Sampling is continued until sufficient data is acquired at each azimuthal position to obtain statistically meaningful averages. In order to facilitate real-time transfer of data from the LDA to the PDP-11 computer the data were transferred in binary format. Once sampling was completed, FORTRAN software written by the authors was used to convert the data to ASCII format and to ensemble-average the data into 1° bins. To obtain the flow field relative to the rotating blade (rotating frame of reference), the blade tip speed was subtracted from the ensemble-averaged mean tangential velocities. It is not necessary to subtract the blade tip speed from the ensemble-averaged mean radial and axial velocities. The data were then transferred electronically to a workstation where software again written by the authors was used for the data analyses and to generate PostScript print files of vector and contour plots. Additional details as well as sample outputs of the raw data are given by Calabrese and Stoots (1989) and Stoots (1989).

Measurements made at each point in the tank yield rotating frame ensemble averages for 360 azimuthal positions. Preliminary results showed that complete symmetry existed for each of the six blades so that data for the same angular positions behind each blade could be combined to yield 60 bins of 1° width to describe the velocity field from one blade to the next. Furthermore, a minimum of 750 velocity realizations per angular bin per sampling location were needed to insure statistically steady values of the mean and root mean square turbulent velocities.

An advantage to this particular measurement technique lies in the fact that since the blades rotate past the sampling volume, it is only necessary to traverse a single r-z plane in the tank to obtain the structure of the trailing vortex system. This plane is located azimuthally halfway between the baffles (that is, 45° away from the baffles). The r and θ components of velocity were obtained by passing the beams in through the bottom of the tank. The z component was acquired through the side wall in the plane of the shaft.

Furthermore, ensemble averaging the data into angular bins diminishes the issue of velocity biasing. Since the burst type LDA is a discrete type of measurement device rather than a continuous type such as hot wire anemometry, it can be susceptible to velocity biasing in flows with large velocity variations. This is due to the greater flux of high vs. low velocity particles through the sampling volume. Researchers have developed various mathematical methods to attempt to eliminate this biasing, but it is unclear if any one method is necessarily better than another, or whether it may introduce some new bias in the measurement. In this work it was felt that no bias correction was necessary, since by phase ensemble averaging the data the disparity is greatly reduced between maximum and minimum velocities for a given bin.

Measurements were made at three impeller rotation rates:

Table 2. Experimental Operating Conditions

	$N=2.33$ rps	$N=3.00$ rps	$N=3.67$ rps
Tip Speed, V_{TIP}, m/s	0.74	0.95	1.16
Reynolds No., *Re*	29,200	37,500	45,800
Dissipation Rate, ϵ_{TANK}, m^2/s^3	0.031	0.065	0.119
$\nu N^2/\epsilon_{TANK} \times 10^4$	1.74	1.38	1.13

2.33 rps, 3.00 rps, and 3.67 rps. Table 2 presents the corresponding tip speeds, tip Reynolds numbers, and average energy dissipation rates. The average energy dissipation rate throughout the tank is simply the power draw per unit mass and estimated using a power number $N_P = P/(\rho N^3 D^5) = 5.0$ (Bujalski et al., 1987).

The grid of measurement locations for the central impeller rotation rate of 3.00 rps is given in Figure 4a. A very dense grid was used to capture the details of the lower vortex formed by the bottom half of the blade both as it wraps around the blade (clinging vortex) and trails behind it (trailing vortex). It was not possible to get closer to the impeller center due to reflections off the impeller hub, disc, and shaft. The sampling grid for the other two impeller speeds is given in Figure 4b.

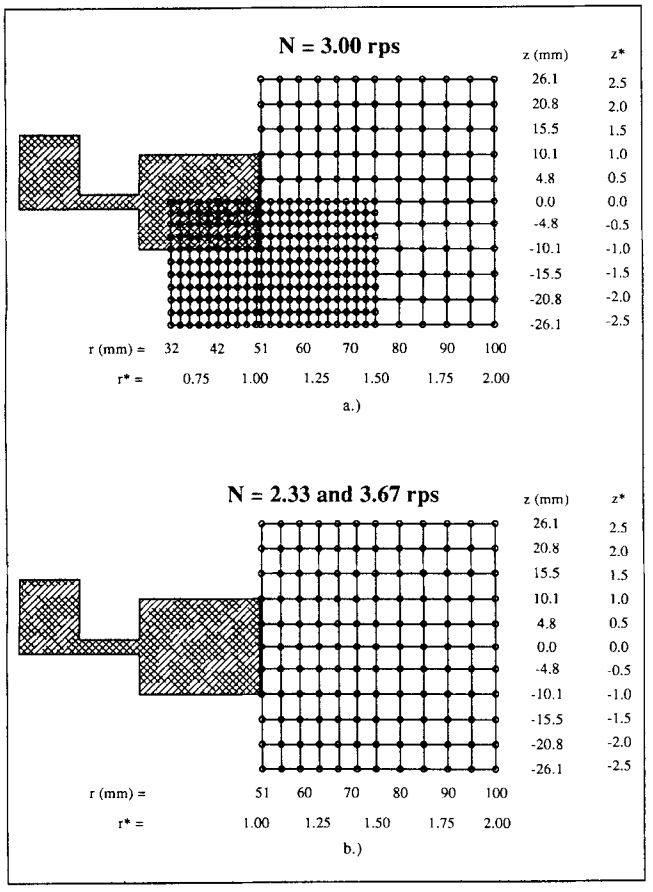

Figure 4. LDA sampling grid.
(a) $N=3.00$ rps; (b) $N=2.33$ and 3.67 rps.

Only the coarse grid outwards from the blade edge was considered since these data were acquired for comparison with the $N = 3.00$ rps results.

Results and Discussion

Figure 4a reveals that measurements were made at 321 grid points for $N = 3.00$ rps. Since each grid point corresponds to 60 angular bins, velocity data were acquired at 19,260 spatial locations within the impeller stream. For each of the other impeller speeds (Figure 4b), measurements were made at 7,920 spatial locations. While such dense sampling allows capture of vortex details, data management and display becomes a formidable task. Vector and contour plots are presented below to succinctly convey information. However, it is only possible to present a small fraction of the graphical results here. Therefore, graphs which show the most important details are presented followed by summaries of the entire data set. Most are for $N = 3.00$ rps. A comprehensive set of graphical results at all three impeller speeds and additional discussion is given by Stoots (1989). Furthermore, two frames of reference have been defined for viewing the data. For purposes of clarity in the ensuing discussion, the symbol V will represent velocities presented in a fixed frame of reference (relative to laboratory coordinates), whereas the symbol U will represent velocities measured in a rotating frame of reference (relative to an impeller blade).

Extent of periodicity

Typical mean radial, tangential, and axial velocities normalized with tip speed for the impeller stream are given as a function of angular position behind the blade in Figures 5 and 6. In these figures, 0° corresponds to the center of the leading blade, and 60° corresponds to the center of the next successive impeller blade. Each curve in these figures shows the periodic variation of mean velocity with azimuthal position for a specific grid point (r, z location). For any given curve, the term "peak velocity" refers to the maximum amplitude. The axial coordinate is nondimensionalized by the blade half width and the radial coordinate by the impeller radius. The reported velocities are absolute velocities relative to fixed coordinates; that is, V_{TIP} has not been subtracted from the tangential velocity. The highest peak mean velocities measured in this study and their locations are tabulated in Table 3. Note that tangential velocities can exceed the blade tip speed, as shown in Figure 5 and Table 3, due to acceleration over the blade. Furthermore, the peak velocities are convected radially and azimuthally away from the blade by the mean flow. However, the most obvious feature of these figures is the periodicity or angular dependence of the flow field. Based on these and the more comprehensive data set reported by Stoots (1989), it can be concluded that the mean velocities display strong periodicity both within the impeller blades ($r^* < 1$) and in the discharge stream. The radial and tangential components display their strongest periodicity along the center plane, $z^* = 0$. The axial mean velocity is nonperiodic at the center plane while exhibiting strong periodicity within the vortices. The extent of periodicity in the radial direction is from $r^* = 0$ to 1.7 and is controlled equally by the radial and tangential components of mean velocity. In the axial direction, periodicity is controlled by the

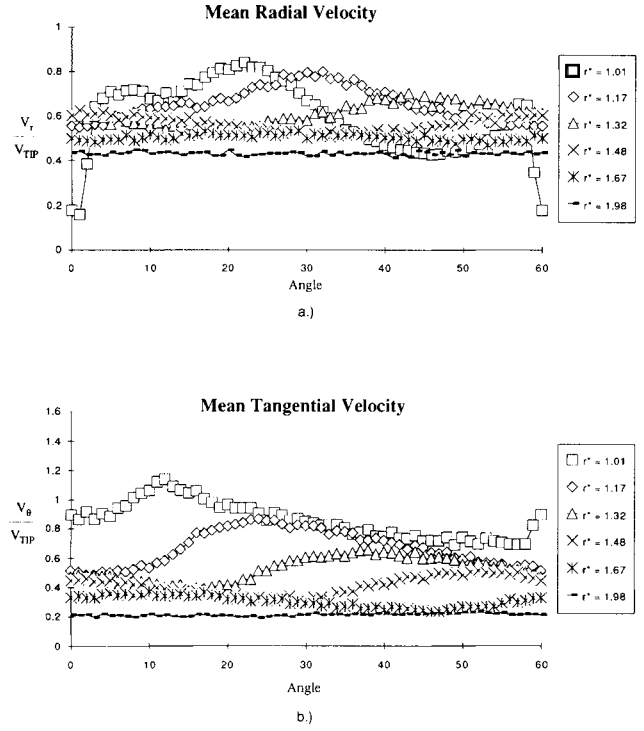

Figure 5. Azimuthal variation of normalized mean velocity at the disc centerplane ($z^* = 0.0$) for various radial positions at $N = 3.00$ rps.

(a) Mean radial velocity; (b) mean tangential velocity.

mean axial velocity and the extent of periodicity is from $z^* = 0$ to ± 2.1.

Results for the other impeller speeds considered are similar in that the mean velocities display strong angular dependence or periodicity, tangential velocities can exceed the blade tip speed, and peak velocities are convected radially and azimuthally away by the mean flow. Furthermore, the spatial extent of periodicity in the flow was found to be the same for the three impeller rotation rates of this study and hence independent of impeller speed. However, some differences were noted. The peak radial mean velocities exhibited complex variations as tip speed was changed. Peaks of mean radial velocity did not exactly scale with tip speed but increased more slowly

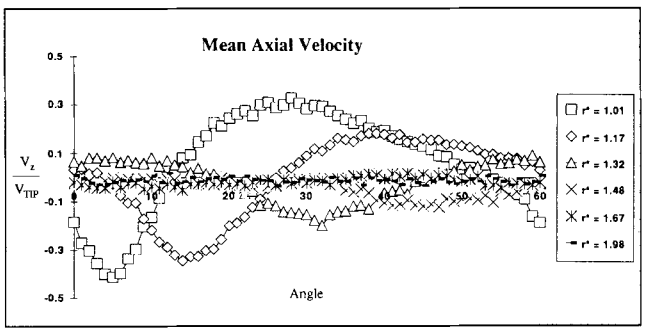

Figure 6. Azimuthal variation of normalized mean axial velocity at $z^* = -0.5$ for various radial positions at $N = 3.00$ rps.

Table 3. Location and Value of Measured Peak Mean Velocities for $N = 3.00$

	Velocity		
	Radial	Tangential	Axial
Peak Value	0.87 V_{TIP}	1.43 V_{TIP}	0.60 V_{TIP}
r^*	1.01	0.87	0.79
θ	22°	10°	13°
z^*	0.0	0.0	−0.48

than impeller speed. Measured values were 0.91 V_{TIP}, 0.87 V_{TIP}, 0.70 V_{TIP} for $N = 2.33$, 3.00, and 3.67 rps, respectively. Also, the peaks of radial mean velocity were convected to larger angular distances with increasing impeller speed ($\theta = 15°$, 22°, and 25°, respectively). Finally, unlike the two other impeller speeds, the axial distribution of mean radial velocity for $N = 3.67$ was not symmetric about the center plane. For $N = 3.67$, the mean radial velocities tended to be stronger above the center plane than below it. The fixed frame radial mean velocity data acquired by Dyster et al. (1993) for turbulent flow conditions also displayed a small systematic variation with impeller speed.

Compared to the radial velocity, the behavior of the mean tangential and axial velocities is less complex. Mean tangential velocities scaled with tip speed whereas the mean axial velocities increased more slowly than impeller speed. It is not possible to compare absolute maximums since the maximums for tangential and axial velocities at $N = 3.00$ rps were measured at locations not sampled at $N = 2.33$ and 3.67 rps.

Mean velocity field

Vector plot renderings of the mean flow field relative to the blade (that is, V_{TIP} is subtracted from the angularly correlated

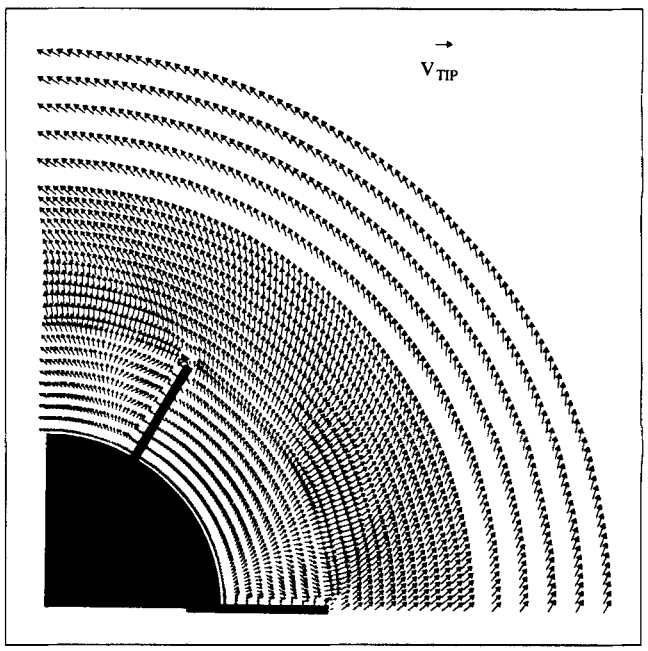

Figure 7. Mean velocity vector plot in disc centerplane ($r - \theta$ plane at $z^* = 0.0$).

Reference arrow has length equal to V_{TIP}; direction of rotation is clockwise.

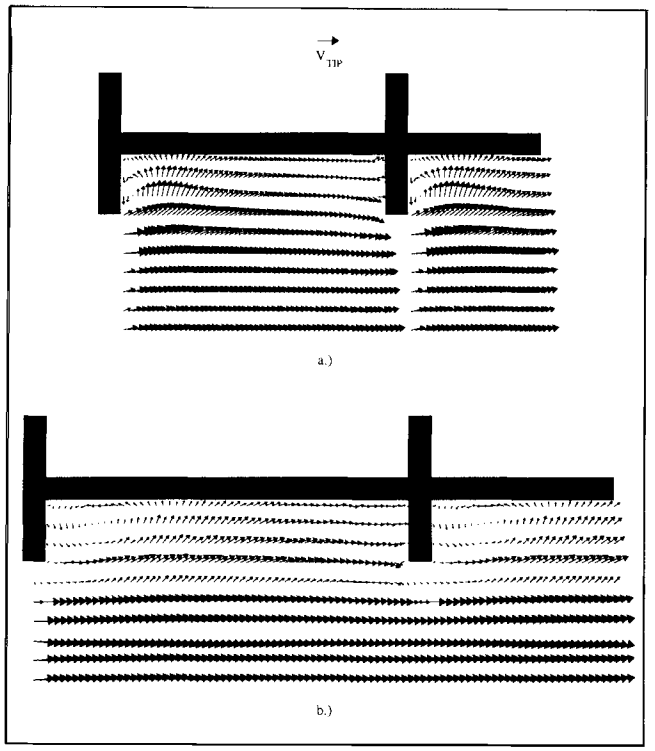

Figure 8. Mean velocity vector plots in θ-z plane for N = 3.00 rps.

Reference arrow has length V_{TIP}; direction of rotation is from right to left. (a) Plane at r^* = 0.75; (b) plane at blade edge (r^* = 1.0).

azimuthal velocity) are presented in Figures 7 through 9 for N = 3.00 rps. Each vector plot depicts one of three possible orthogonal planes. Figure 7 represents a r-θ plane or plane of constant z^*, and Figure 8 constitutes θ-z planes or planes of constant r^*. The exact location of each plane can be determined from Figure 4. Figure 9 gives r-z planes or planes of constant θ. Although the ensemble averaging of quantities was only done over 60°, about 90° of data are presented in Figures 7 and 8. The first 30° of data is repeated for the region 60° to 90° to better visualize the characteristics of the flow field as it passes around the blade. In Figure 7, the blade may be thought of as rotating clockwise, and in Figure 8 the blade is moving from right to left. Finally, the impeller is drawn to scale in the flow field and the reference arrow has magnitude V_{TIP}. It should be noted that Figures 8a and 8b are drawn to the same scale. The plane of Figure 8b is greater in width than that of Figure 8a, being at a greater radial distance from the origin. The plane of Figure 8a passes through the blades. Velocity vectors directly below the blades are not shown since the r and θ components could not be acquired through the tank bottom due to laser beam reflections off the blades. In the discussion that follows, that portion of the vortex which wraps around the blade will be referred to as the clinging vortex, while that which is away from the blade is termed the trailing vortex (Figure 2b).

Figure 7 displays mean velocities in the impeller disc or center plane where the two vortices meet. It includes the region where the strongest mean tangential velocities were recorded. The strong recirculation zone caused by the clinging vortices behind

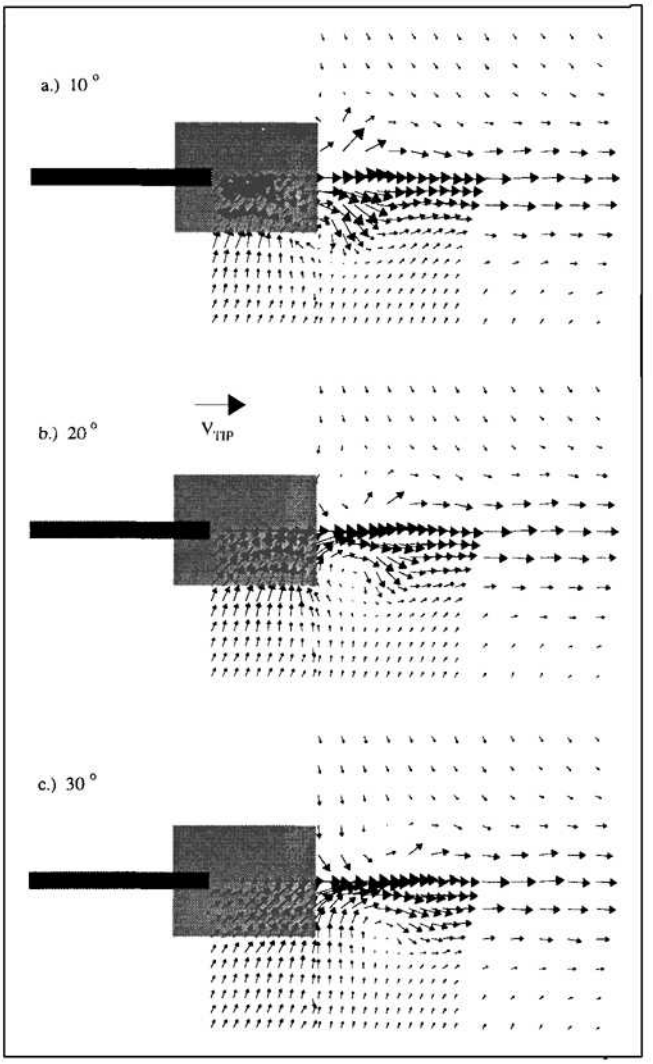

Figure 9. Mean velocity vector plots in r-z plane for N = 3.00 rps.

Reference arrow has length V_{TIP}; direction of rotation is into page away from viewer. Arrows are behind the blade at (a) 10°; (b) 20°; (c) 30°.

the impeller blade is responsible for the tangential velocities exceeding the blade velocity in this region. The axis of the clinging vortex first parallels the horizontal blade edge at r^* = 0.75 (Figure 8a) where the vortex extends to about 7° behind the blade edge. The vortex diameter grows as one moves radially outwards, extending to about 15° by the outer blade edge (Figure 8b). Figure 9 depicts the mean trailing vortex flow field for various angular positions behind the turbine blade. Several observations may be made. For angular displacements of 20° and more behind the leading blade the trailing vortex no longer exhibits a complete circulation loop. This agrees well with Yianneskis et al. (1987) who reported vortical structures for displacements up to 20°. Another observation is that the trailing vortex maintains its identity to about a 30° lag or 2 blade widths beyond the outer blade tip. Here the mean radial velocities are largest and the angularly resolved pumping capacity displays a maximum. The characteristic radial jet of the Rushton turbine is a consequence of fluid entrainment into

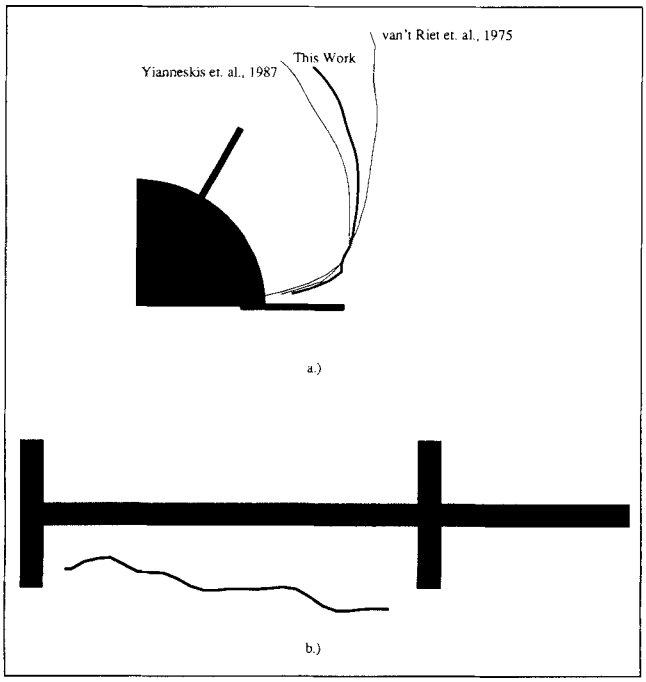

Figure 10. Mean axis of lower vortex.

(a) r-θ plane; direction of rotation is clockwise; (b) θ-z plane; direction of rotation is from right to left.

the vortex and follows the vortex axis. Due to this, the radial jet actually lags behind the blade. Fixed frame results may mislead some to believe that it is pushed out in front of the blade.

Figure 9 shows that the coarse grid of Figure 4 is insufficient to resolve the details of the vortex structure. Therefore, a direct comparison of the upper and lower vortices at $N = 3.00$ rps or a comparison of results with those for the other two impeller speeds is difficult. However, to a first approximation, the general features of the mean flow field are the same for the range of impeller speeds studied. This is the case despite the detailed differences discussed above. The following conclusions are therefore independent of impeller speed.

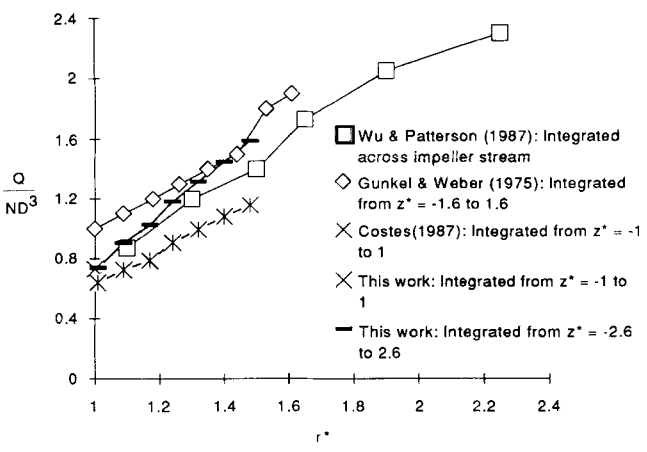

Figure 11. Radial variation of pumping number.

Comparison of results of this study at $N = 3.00$ rps with those of other studies.

Remains of the mean vortex structure can be detected to about 55°. The diameter of the trailing vortex does not grow substantially from the outer blade edge to where it breaks down. At 30° behind the blade its diameter is slightly less than one blade width. A comparison of the hub side and open side (upper and lower) vortices showed that the hub side vortex was less structured. Peak mean velocities are stronger for the hub side but of a smaller spatial extent. This may be due to the presence of the hub and possibly the free surface. Pumping capacities above and below the center plane are about the same.

The mean axis of the lower vortex was determined by locating its center of rotation from the mean velocity data and then smoothing the positions through use of a cubic spline approximation (Gerald, 1978). A comparison of the vortex axis in the r-θ plane, calculated in this work for $N = 3.00$ rps with those of Yianneskis et al. (1987) and van't Riet et al. (1975), is presented in Figure 10a. Differences in the particular experiments may explain discrepancies in the vortex axes. Van't Riet et al. utilized larger (0.5 mm dia) polystyrene particles to visualize the flow field, thus possibly introducing some inertial effects. The impeller utilized by Yianneskis et al. contained a hub on both the top and bottom of the disc and was located with a clearance of T/3 from the bottom. The impeller used in this work contained a considerably larger hub, but only on the upper surface of the disc. These hub differences may explain why Yianneskis et al. (1987) found symmetry of mean velocity relative to the disc plane and why our upper vortex was less structured. The axis of the lower vortex at $N = 3.00$ rps in the θ-z plane is shown in Figure 10b. The axis was found to be 8° to 10° below the horizontal. For the other two impeller speeds of this study, the vortex axes were virtually the same as those for $N = 3.00$ rps. While our vortex axis is different than that of van't Riet et al. (1975), the conclusion remains that for fully turbulent flow the axis is independent of impeller speed.

Impeller pumping capacity

Profiles of pumping capacity in the form of pumping number (Q/ND^3) as a function of radial position are displayed in Figure 11 for this work at $N = 3.00$ rps and for other studies. For this work the pumping capacity, which is a fixed frame quantity, was obtained by integrating azimuthally to obtain fixed frame mean radial velocities and then vertically over the radial jet:

$$Q = 6 \int_{-z^*}^{z^*} dz. \int_0^{60^\circ} U_r(r,\theta,z)\, r\, d\theta \qquad (1)$$

$U_r(r, \theta, z)$ is the angularly correlated radial component of velocity. The factor 6 appears since the azimuthal integration is only carried out between two blades ($0° \le \theta < 60°$). As discussed above, using angularly resolved data for the calculation diminishes the issue of velocity biasing and leads to more accurate values for pumping capacity. The integration was carried out for two sets of axial limits ($z^* = \pm 1.0$ and $z^* = \pm 2.6$) and at several radial distances outward from the blade edge. The first set of limits corresponds to integrating across the blade width. The justification for the second set of inte-

gration limits is that the region of positive mean radial velocity extends across the entire span of axial grid locations used in this study. Hence, to encompass this entire radial jet the limits of integration need to extend across the entire grid.

The pumping numbers of this study are in reasonable agreement with those of other workers for fully turbulent conditions. The higher values reported by Gunkel and Weber (1975) have been discussed above. The lower values of Wu and Patterson (1987) may be attributable to their impeller clearance of T/3. Dyster et al. (1993) and Cooper and Wolf (1968) reported pumping numbers at the outer blade edge ($r^* = 1$) of 0.78 and 0.8, respectively. The results for the two sets of axial limits used in this study diverge with increasing radial position, due to the entrainment of fluid into the radial jet as it moves radially outward from the blade, thereby increasing the radial jet flow rate. While the data presented in Figure 11 are for $N = 3.00$ rps, the pumping number was also calculated as a function of radial position for the other two impeller speeds of this study. Comparison revealed less than a 10% variation in pumping number with impeller speed but no predictable trends. Further discussion may be found in Stoots (1989).

Deformation rates

The stress acting on a fluid element can be related to the finite components of the rate of deformation tensor Δ which are written in terms of mean velocities and for cylindrical coordinates in Table 4. In simple flows the terms in Table 4 may reduce to a single finite velocity gradient. In the impeller stream all of the components of Δ are finite so that inspection of individual mean velocity gradients is cumbersome and does not provide an adequate picture of the deformation field. In a turbulent flow it is not possible to measure instantaneous deformation rates via LDA so that neither the mean deformation rate or a direct measure of the energy dissipation rate can be obtained. Nevertheless, it is useful to consider gradients of mean velocity, or in a complex flow, some measure of the magnitude of the mean velocity gradients which represents deformation. Such a measure can be obtained by taking the scalar product of the deformation rate tensor in terms of mean velocities (Table 4) with itself. The resulting deformation rate is:

$$\dot{\delta} = \sqrt{\frac{1}{2}\,\Delta:\Delta} \tag{2}$$

Again it is noted that $\dot{\delta}$ is not the mean deformation rate but rather a measure of the magnitude of the deformation rate due to mean velocity gradients in the flow field. It provides a measure of the variations in mean velocity in the system and elucidates regions of intense mean velocity changes and turbulence energy production. A practitioner may refer to it as a measure of total mean shear or the magnitude of the mean velocity gradients.

$\dot{\delta}$ may be nondimensionalized with the impeller speed to yield:

$$\dot{\delta}^* = \frac{\dot{\delta}}{N} \tag{3}$$

A cubic spline approximation (Gerald, 1978) was employed to calculate each of the gradients of mean velocity depicted in Table 4.

Table 4. Components of the Rate of Deformation Tensor Δ in Cylindrical Coordinates

$\Delta_{rr} = 2\dfrac{\partial U_r}{\partial r}$	$\Delta_{r\theta} = \Delta_{\theta r} = r\dfrac{\partial}{\partial r}\left(\dfrac{U_\theta}{r}\right) + \dfrac{1}{r}\dfrac{\partial U_r}{\partial \theta}$
$\Delta_{\theta\theta} = 2\left(\dfrac{1}{r}\dfrac{\partial U_\theta}{\partial \theta} + \dfrac{U_r}{r}\right)$	$\Delta_{\theta z} = \Delta_{z\theta} = \dfrac{\partial U_\theta}{\partial z} + \dfrac{1}{r}\dfrac{\partial U_z}{\partial \theta}$
$\Delta_{zz} = 2\dfrac{\partial U_z}{\partial z}$	$\Delta_{zr} = \Delta_{rz} = \dfrac{\partial U_z}{\partial r} + \dfrac{\partial U_r}{\partial z}$

Contours of deformation rate in the r-θ plane are given in Figure 12 for $N = 3.00$ rps. Figure 12a corresponds to a horizontal plane which approximately passes through the center of the bottom vortex. The regions of highest deformation

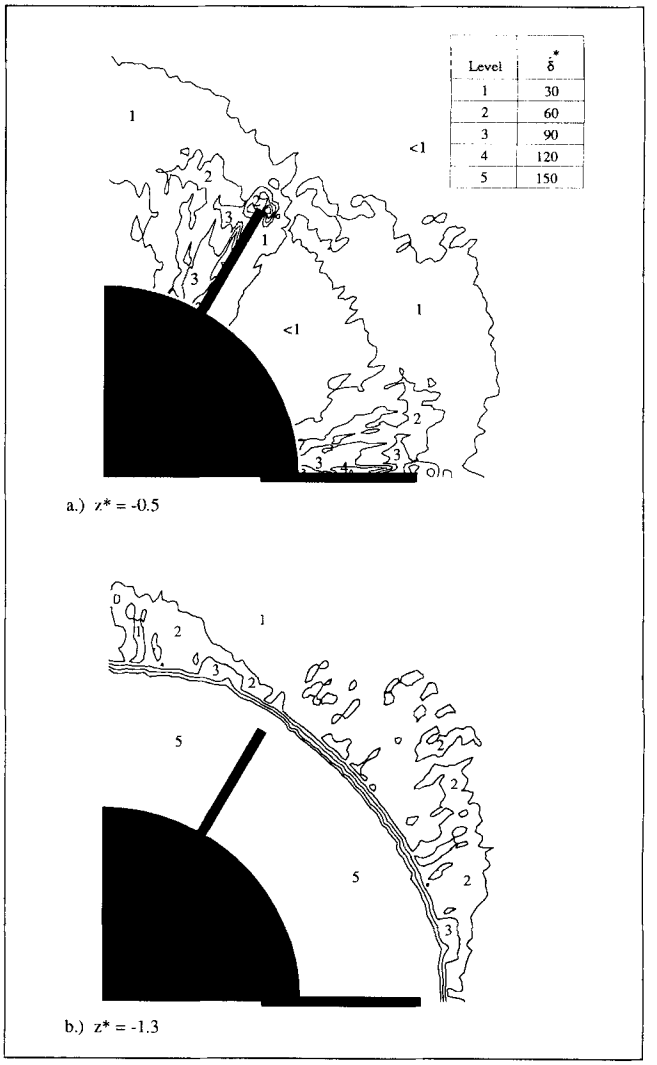

Figure 12. Normalized deformation rate contour plots in the r-θ plane for $N = 3.00$ rps.

Direction of rotation is clockwise. (a) Within the bottom vortex at $z^* = -0.5$; (b) below the bottom blade edge at $z^* = -1.3$ where contours between the blades are not shown for clarity.

are in the clinging vortex and along the blade edges. Typical values of deformation rate for the clinging vortex are 60 to 200 times the impeller rotation speed. On the blade edges, $\dot{\delta}^* = 150$ is a typical value. Wichterle et al. (1984) found that for water, shear rates on the front of the blades were as high as 1,200 times the impeller speed. However, their electrochemical technique allowed them to measure shear rates directly on the blade surface and not a small distance away. Figure 12a further reveals that deformation rates are weaker for the trailing (vs. clinging) vortex but that contours generally follow the vortex axis. Both the upper and lower trailing vortices and breakdown regions are characterized by $20 < \dot{\delta}^* < 60$.

Figure 12b indicates that there is a narrow region $z^* = -1.3$ and $r^* = 1.1$ where deformation rates are moderately strong ($10 < \dot{\delta}^* < 50$), vary rapidly with radial distance and are independent of angular position. The reason for this can be seen by reference to Figures 8b and 9. Below this region the fluid is moving upward into the vortex, but the blade is rapidly moving away from it in a tangential sense. In this region the fluid feels the presence of the blade as it is accelerated tangentially to move with the blade. Since this region has well defined mean velocity gradients and is away from the impeller swept volume, it may be a good location to introduce a feed stream if rapid mixing is required.

Figure 13 presents the deformation field at $N = 3.00$ rps in the θ-z plane at the outer blade edge. It was only possible to calculate deformation rates below the disc center plane and for this impeller speed, because data at grid points interior to the blade edges were needed to obtain realistic values of $\dot{\delta}^*$ in this grid plane (see Figure 4). The results corroborate the discussions associated with Figures 12a and 12b. At this radial position the region of highly organized angularly independent mean velocity gradients is more extensive and deformation rates are much higher. The narrow region of strong deformation actually extends from about $r^* = 0.8$ to $r^* = 1.2$.

Figure 14 presents the deformation field in the r-z plane at 15° behind the blade for the three impeller speeds of this study. A comparison of Figures 14a and 14c shows that normalized deformation rates are almost independent of impeller speed and are similar above and below the impeller disc plane. The results at 2.33 rps show some lack of symmetry that does not exist at 3.67 rps. Therefore, there is a weak dependence of $\dot{\delta}^*$ on impeller speed. Some differences in normalized mean velocities at the different impeller speeds were discussed above. Therefore, it is not surprising that differentiated data would also show some differences.

Figure 14b gives deformation rates at 3.00 rps for the region of the fine grid of Figure 4a. At first glance, these results appear to be somewhat different than those of Figures 4a and 4c, but this is actually not the case. The contours are not as "smooth" due to the finer grid but show the same general trends radially outward from the blade. The discrepancies below the outer blade tip are due to the behavior of the cubic spline algorithm at the grid edges. Since velocity data were not available for $r^* < 1$, the derivative of the estimated variable (in this case velocity gradient) was set to zero for $r^* < 1$ and $z^* < -1$ so that $\dot{\delta}^*$ was forced to become independent of r^* close to the upper and lower blade tips. This was not necessary for $N = 3.00$ rps so the region of $\dot{\delta}^* = 5$ was continuously extended below the blade. Figure 14b shows that on the plane of the vertical blade edge, the deformation rate remains sig-

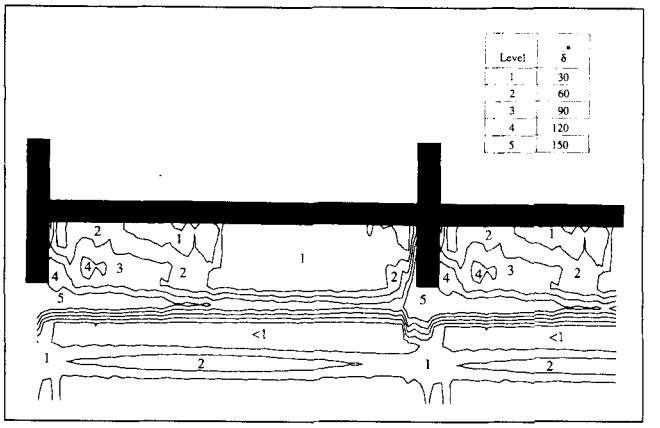

Figure 13. Normalized deformation rates below the disc centerplane at the outer blade edge ($r^* = 1.0$) for $N = 3.00$ rps.

Direction of rotation is from right to left.

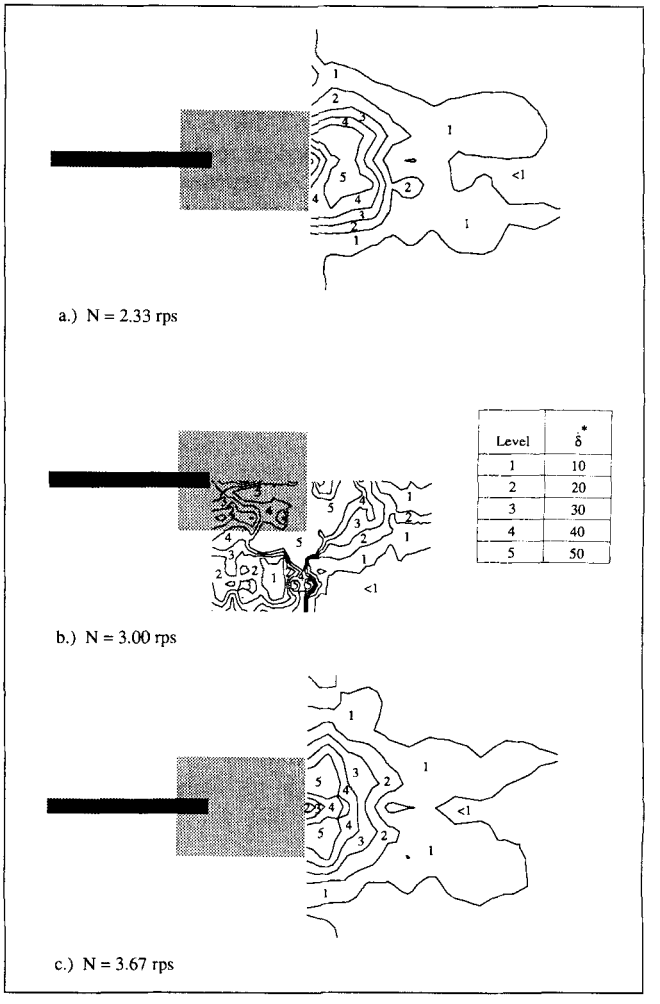

Figure 14. Normalized deformation rate contour plots in the r-z plane at 15° behind the blade vs. impeller speed.

Direction of rotation is into the page away from the viewer. Comparison of results at (a) 2.33 rps; (b) 3.00 rps; (c) 3.67 rps.

nificant even below the bottom edge of the lower vortex. Deformation rates on the inner side of the vortex are not substantially different than those on the outer side.

Energy dissipation due to mean velocity gradients

For an incompressible Newtonian fluid the energy dissipation rate per unit mass is given by:

$$\epsilon_\Delta = \frac{1}{\rho}\,\tau:\,\nabla \mathbf{U} = \frac{1}{2}\,\nu \mathbf{\Delta}:\mathbf{\Delta} = \nu \dot{\delta}^2. \tag{4}$$

Therefore, the deformation rate data can be used to estimate the energy dissipation rate due solely to mean velocity gradients. In a turbulent flow, energy dissipation is due to instantaneous velocity gradients, which are expected to be much larger in magnitude than the mean gradients. However, it is useful to see what magnitude of dissipation rate can be obtained by considering only the deformation field due to mean velocity gradients. ϵ_Δ can be normalized by the mean energy dissipation rate for the tank (given in Table 2) so that Eq. 4 yields:

$$\epsilon_\Delta^* = \frac{\epsilon_\Delta}{\epsilon_{TANK}} = \frac{\nu N^2}{\epsilon_{TANK}}\,\dot{\delta}^{*2}. \tag{5}$$

Values of $\nu N^2/\epsilon_{TANK}$ are given in Table 2. Equation 5 shows that ϵ_Δ^* is not independent of impeller speed. However, since $\dot{\delta}^*$ is approximately independent of impeller speed, ϵ_Δ^* can be estimated using the contour plots of Figures 12 to 14 or the more extensive graphical tabulations of Stoots (1989). Calculations at $N = 3.00$ rps show that on the outer edges of the clinging vortex, along the blade edge and in the narrow region near $z^* = -1.3$ and $0.8 < r^* < 1.2$, ϵ_Δ^* can range from 3 to 10. That is, if the turbulent nature of the flow field were not considered, there are still isolated regions of the flow field where the local dissipation based on deformation rates due to mean velocity gradients exceed the tank power draw per unit mass by as much as an order of magnitude. Based on fixed frame velocity data, Wu and Patterson (1989) estimated that maximum turbulent energy dissipation rates in the trailing vortices were about 20 times greater than ϵ_{TANK}.

Summary and Conclusions

While certain aspects of the normalized velocity and deformation rate fields vary with impeller speed, the essential details are independent of N over the range of conditions studied. The extent of periodicity extends to $r^* = 1.7$ and $z^* = \pm 2.1$. There is some lack of symmetry in the mean velocity above vs. below the disc centerplane, possibly due to the presence of the relatively large hub on the top side of the impeller. The diameter of the clinging vortex grows as it moves outward from the blade. The trailing vortex is about one blade width in diameter and extends to about 30° behind the blade. Remnants of mean velocity structure extend to about 55°. The radial jet lags the blades and is a result of entrainment of fluid into the vortices.

Deformation rates based on gradients of the mean velocity can exceed the impeller rotational frequency by as much as two orders of magnitude close to blade edges and in a narrow region from $r^* = 0.8$ to 1.2 just beyond and away from the outer vertical blade edge. In this region deformation rates are independent of angular position. While the mean velocity field is somewhat lacking in vertical symmetry, the deformation field is more nearly symmetric. Near the blade edges, energy dissipation rates calculated solely from mean velocity gradients can exceed the tank power draw per unit mass by up to an order of magnitude.

While measuring the mean velocity field on a relatively dense grid as done here yields important physical insights into impeller stream hydrodynamics, it does not provide the entire picture. The vortices create the intense turbulent field essential to mixing processes. Measurements of the turbulence characteristics of the flow field relative to the rotating blade are free of pseudoturbulence due to flow field periodicity, and therefore provide key information to a complete understanding of the impeller stream. The LDA technique described here provides the data set required to quantify the turbulence. The turbulent velocity field will be reported in a future article.

Acknowledgment

The authors are grateful for partial support of this work from the Minta Martin Fund for Aeronautical Research of the University of Maryland, National Science Foundation Grant No. CBT-8612020 and through the Long Term Research Initiative Program under DOE Idaho Operations Office Contract DE-AC07-76IDO1570.

Notation

D = impeller diameter, m
N = impeller speed, revolutions per second
P = power input into the tank, W
Po = power number, $P/\rho N^3 D^5$
Q = volumetric flow rate, m^3/s
Re = Reynolds number, ND^2/ν
U = velocity in rotating frame of reference, m/s
V = velocity in fixed frame of reference, m/s
r = radius of measurement point, m
r^* = dimensionless radial coordinate, $2r/D$
T = tank diameter, m
W = impeller blade width, m
z = axial distance from impeller center plane, m
z^* = dimensionless axial coordinate, $2z/W$

Greek letters

$\dot{\delta}$ = magnitude of deformation rate due to mean velocity gradients, s^{-1}
Δ = rate of deformation tensor, s^{-1}
ϵ = energy dissipation rate, m^2/s^3
θ = azimuthal position of measurement, (°)
ρ = density, kg/m^3
ν = kinematic viscosity, m^2/s

Subscripts

r = radial direction
θ = azimuthal direction
z = axial direction
TANK = average throughout tank
TIP = impeller blade tip
Δ = due to gradients of mean velocity

Literature Cited

Bujalski, W., A. W. Nienow, S. Chatwin, and M. Cooke, "The Dependency on Scale of Power Numbers of Rushton Disc Turbines," *Chem. Eng. Sci.*, **42**, 317 (1987).

Calabrese, R. V., and C. M. Stoots, "Flow in the Impeller Region of a Stirred Tank," *Chem. Eng. Prog.*, **85**(5), 43 (1989).
Cooper, R. G., and D. Wolf, "Velocity Profiles and Pumping Capacities for Turbine Type Impellers," *Can. J. Chem. Eng.*, **46**, 94 (1968).
Dyster, K. N., E. Koutsakos, Z. Jaworski, and A. W. Nienow, "An LDA Study of the Radial Discharge Velocities Generated by a Rushton Turbine: Newtonian Fluids, $Re \geq 5$," *Trans. I. Chem. E.*, **A71**, 11 (1993).
Gerald, C. F., *Applied Numerical Analysis*, Addison Wesley Publishing, Reading, MA (1978).
Gunkel, A. A., and M. E. Weber, "Flow Phenomena in Stirred Tanks: I. The Impeller Stream," *AIChE J.*, **21**, 931 (1975).
Melling, A., and J. H. Whitelaw, "Turbulent Flow in a Rectangular Duct," *J. Fluid Mech.*, **78**, 289 (1976).
Mujumdar, A. S., B. Huang, D. Wolf, M. E. Weer, and W. S. M. Douglas, "Turbulence Parameters in a Stirred Tank," *Can. J. Chem. Eng.*, **48**, 475 (1970).
Rao, M. A., and R. S. Brodkey, "Continuous Flow Stirred Tank Turbulence Parameters in the Impeller Stream," *Chem. Eng. Sci.*, **27**, 137 (1972).
Ranade, V. V., and J. B. Joshi, "Flow Generated by a Disc Turbine: I. Experimental," *Trans. I. Chem. Eng.*, **A68**, 19 (1990).
Stoots, C. M., "The Velocity Field Relative to a Rushton Turbine Blade," PhD Thesis, Univ. of Maryland, College Park (1989).
van't Riet, K., and J. M. Smith, "The Behavior of Gas-Liquid Mixtures Near Rushton Turbine Blades," *Chem. Eng. Sci.*, **28**, 1031 (1973).
van't Riet, K., and J. M. Smith, "The Trailing Vortex System Produced by Rushton Turbine Agitators," *Chem. Eng. Sci.*, **30**, 1093 (1975).
van't Riet, K., W. Bruijn, and J. M. Smith, "Real and Pseudo-Turbulence in the Discharge Stream from a Rushton Turbine," *Chem. Eng. Sci.*, **31**, 407 (1976).
Wichterle, K., M. Kadlec, L. Zak, and P. Mitschka, "Shear Rates on Turbine Impeller Blades," *Chem. Eng. Commun.*, **26**, 25 (1984).
Wu, H., and G. K. Patterson, "Laser-Doppler Measurements of Turbulent-Flow Parameters in a Stirred Mixer," *Chem. Eng. Sci.*, **44**, 2207 (1987).
Yianneskis, M., Z. Popiolek, and J. H. Whitelaw, "An Experimental Study of the Steady and Unsteady Flow Characteristics of Stirred Reactors," *J. Fluid Mech*, **175**, 537 (1987).

Manuscript received Sept. 27, 1993, and revision received Feb. 18, 1994.